# van der Waals multiferroic tunnel junctions based on sliding multiferroic layered $VSi_2N_4$

Yulin Feng,[1] Jiangchao Han,[2] Kun Zhang,[2] Xiaoyang Lin,[2] Guoying Gao,[3,*] Qing Yang,[4,†] and Sheng Meng[4,5,‡]

[1]*College of Physics and Electronic Science and Hubei Key Laboratory of Photoelectric Materials and Devices, Hubei Normal University, Huangshi 435002, China*

[2]*Fert Beijing Institute, MIIT Key Laboratory of Spintronics, School of Integrated Circuit Science and Engineering, Beihang University, Beijing 100191, China*

[3]*School of Physics and Wuhan National High Magnetic Field Center, Huazhong University of Science and Technology, Wuhan 430074, China*

[4]*Beijing National Laboratory for Condensed Matter Physics and Institute of Physics, Chinese Academy of Sciences, Beijing 100190, China*

[5]*School of Physical Sciences, University of Chinese Academy of Sciences, Beijing 100049, China*

(Received 20 December 2023; revised 30 January 2024; accepted 5 February 2024; published 27 February 2024)

Multiferroic tunnel junctions (MFTJs) have attracted considerable attention due to their multifunctional properties, which are valuable for nonvolatile memory devices. The recent advancements in van der Waals (vdW) multiferroic materials, combining ferromagnetic and ferroelectric properties, provide an excellent platform for exploring MFTJs at the atomic scale. In this study, we employ a combination of nonequilibrium Green's function and density functional theory to theoretically investigate the spin-dependent transport properties of vdW MFTJs, which consist of metal electrodes and sliding multiferroic layered $VSi_2N_4$ barrier layers. Our findings demonstrate that asymmetric Ag(111)/bilayer-$VSi_2N_4$/Au(111) MFTJs can exhibit multiple nonvolatile resistance states by manipulating the ferroelectric polarization and magnetization alignment of the bilayer $VSi_2N_4$, achieving maximum tunneling magnetoresistance (TMR) and tunneling electroresistance (TER) ratios of up to $1.01 \times 10^5$% and 37.3%, respectively. More intriguingly, the TER ratio can be further increased to 448.3% by employing left and right symmetric Au(111) electrodes and trilayer $VSi_2N_4$ barrier layers. Additionally, we reveal that layered $VSi_2N_4$ possesses intrinsic multiferroicity with the coexistence of the out of plane ferroelectricity and interlayer *A*-type antiferromagnetism. Through an analysis of electronic structure and Berry curvature, we elucidate the coupling between ferroelectricity and antiferromagnetism via a ferrovalley, enabling electrically controlled magnetism in the bilayer $VSi_2N_4$ by interlayer sliding. Our results demonstrate that giant TMR, large TER, and multiferroic coupling can coexist in layered $VSi_2N_4$, with potential applications in other vdW layered multiferroics. The controllable interlayer sliding of vdW MFTJs offers promising opportunities for the design of next-generation logic and memory devices.

DOI: 10.1103/PhysRevB.109.085433

## I. INTRODUCTION

The emergence of multiferroic tunnel junctions (MFTJs), by combining the two different magnetization alignments of the ferromagnetic electrodes with ferroelectric ultrathin films as the tunnel barrier, has shown promise in addressing the challenges faced by conventional silicon-based semiconductor devices [1–3]. MFTJs exhibit multiple nonvolatile resistance states by combining the tunnel magnetoresistance (TMR) effect from magnetic tunnel junctions (MTJs) [4,5] and the tunnel electroresistance (TER) effect from ferroelectric tunnel junctions (FTJs) [6,7]. The key to the functionality of MFTJs lies in the utilization of multiferroic materials that possess both ferroelectric (FE) and ferromagnetic (FM) properties [8,9]. Traditional MFTJs typically involve ferroelectric perovskite oxides sandwiched between magnetic composite/alloy films [10,11]. However, the interface between different crystals in these structures can introduce significant contacting resistance and high energy consumption, which can adversely affect device performance. To address these challenges, researchers have turned to two-dimensional (2D) van der Waals (vdW) materials as a promising solution [12,13]. These materials have atomic thickness, uniform surfaces, and free dangling bonds, making them suitable for constructing vdW MFTJs in a sandwichlike heterostructure [14–21]. This approach has opened up new opportunities for low-power device applications in the nonvolatile memory industry.

Recent advancements in the field have demonstrated that interlayer sliding of 2D materials can effectively regulate various properties, including ferroelectricity [22,23], ferromagnetism [24,25], multiferroicity [26,27], and valley polarization [28,29]. The weak interlayer vdW interactions have enabled the emergence of vertical sliding ferroelectricity in bilayer hexagonal BN [30,31] and the coupling of ferroelectricity and antiferromagnetism through a ferrovalley in bilayer $VS_2$ [32]. These findings have enabled electronic control of magnetism and paved the way for new device paradigms based on four logic states. Thus, the rapid development of vdW sliding multiferroic materials have provided an ideal platform for exploring MFTJs at the atomic scale. A novel class of 2D materials known as $MA_2Z_4$ ($M$ = a transition

*guoying_gao@mail.hust.edu.cn
†yang_qing@iphy.ac.cn
‡smeng@iphy.ac.cn

 

metal; $A$ = Si, Ge; $Z$= N, P, As) has recently been proposed and synthesized [33]. Moreover, the monolayer $VSi_2N_4$ has exhibited ferromagnetic, two-valley semiconductor behavior with valley splittings resulting from magnetization and significant spin-orbit coupling [34,35]. Additionally, semiconducting $MoA_2N_4$ bilayers and multilayers have demonstrated robust out-of-plane ferroelectricity via interlayer sliding [36]. Furthermore, the bilayer $VSi_2P_4$ has been identified as a multiferroic material, offering the potential for layer-polarized anomalous Hall effect in valleytronic vdW bilayers through interlayer sliding [37]. These excellent properties and multiferroic couplings make such materials an ideal platform for exploring novel MFTJs at the atomic scale.

In this paper, we combine the concepts of sliding multiferroics and MFTJs to study the manipulation of TMR and TER effects in layered $VSi_2N_4$ through interlayer sliding. We demonstrate that the bilayer $VSi_2N_4$ exhibits intrinsic multiferroicity, characterized by the coexistence of out of plane ferroelectricity and interlayer $A$-type antiferromagnetism. Through the analysis of electronic structure and Berry curvature (BC), we reveal that ferroelectricity and antiferromagnetism can be coupled through a ferrovalley, enabling electrically controlled magnetism in the bilayer $VSi_2N_4$ via interlayer sliding. Furthermore, we theoretically investigate the spin-dependent electronic transport properties of asymmetric Au(111)/bilayer-$VSi_2N_4$/Ag(111) vdW MFTJs and symmetric Au(111)/trilayer-$VSi_2N_4$/Au(111) vdW MFTJs. These devices, owing to the multiple polarization states of the layered $VSi_2N_4$, exhibit high tunability through interlayer sliding. Our results reveal a significant TMR ratio of up to $5.68 \times 10^3$% in the MFTJs by altering the magnetic orders of the trilayer $VSi_2N_4$ from parallel configuration (PC) to antiparallel configuration (APC) arrangement, as well as a large TER ratio of up to 448.3% through ferroelectric-antiferroelectric (FE-AFE) order transitions of the trilayer $VSi_2N_4$. The innovative design of vdW MFTJs based on layered $VSi_2N_4$ can be extended to other sliding multiferroics, offering new avenues for further experimental exploration of vdW MFTJs. This research opens up exciting possibilities for the development of next-generation devices that harness the unique properties of 2D materials and enable advanced functionality in areas such as nonvolatile memory devices.

## II. COMPUTATIONAL METHODS

The structural optimization, total energy, and band structure calculations of all systems are performed by using the projected augmented-wave method as implemented in the Vienna *ab initio* simulation package (VASP). The generalized gradient approximation (GGA) [38] with Perdew-Burke-Ernzerhof (PBE) [39] is used to treat the exchange-correlation interaction. The effective $U$= 3 eV is adopted on the $d$ orbitals of the V atoms. The kinetic energy cutoff is set to be 500 eV. A vacuum space of 15 Å is considered to avoid interaction between neighboring slabs. All atoms are fully relaxed until the energy ($10^{-6}$ eV) and force (0.01 eV/Å) convergence criteria are reached. The Grimme-D2 type of vdW force correction is included in our calculations [40,41]. Centered $k$-mesh points of $15 \times 15 \times 1$ are used for the structural optimization and total-energy estimation [42]. We employ VASPBERRY to calculate the Berry curvature [43]. Ferroelectric polarization is evaluated using the Berry phase approach [44]. The energy barrier of ferroelectric switching is investigated using the nudged elastic band (NEB) method [45].

The spin transport properties are calculated based on the density functional theory combined with the nonequilibrium Green's function method implemented in the ATOMISTIX TOOLKIT (ATK) package [46–48]. The GGA with PBE functional is adopted for the electronic exchange correlation functional. Since the effective $U$ has little effect on the transport properties in our simulations, the effective $U$ is not considered in the equilibrium transport calculations. The spin-dependent tunneling current $I_\sigma$ and conductance $G_\sigma$ can be obtained by the Landauer-Büttiker formula [49,50],

$$I_\sigma = \frac{e}{h}\int T_\sigma(E)[f_L(E) - f_R(E)]dE, \tag{1}$$

$$G_\sigma = \frac{e^2}{h}T_\sigma, \tag{2}$$

where $\sigma$ represents the spin index ($\uparrow$, $\downarrow$), $e$ denotes the electron charge, $h$ is the Planck's constant, $T_\sigma$ $(E)$ is the spin-resolved transmission coefficient, and $f_{L(R)}$(E) is the Fermi-Dirac distribution function of the left (right) electrode.

In the equilibrium state, the TMR can be calculated by [51]

$$\mathrm{TMR} = \frac{G_P - G_{AP}}{G_{AP}} = \frac{T_P - T_{AP}}{T_{AP}}, \tag{3}$$

where $T_{P/AP}$ are the total transmission coefficient at the Fermi level in the P and AP magnetic states, respectively. Similarly, the TER ratio is defined as [52]

$$\mathrm{TER} = \frac{|G_\uparrow - G_\downarrow|}{\min(G_\uparrow, G_\downarrow)} = \frac{|T_\uparrow - T_\downarrow|}{\min(T_\uparrow, T_\downarrow)}, \tag{4}$$

where $T_{\uparrow/\downarrow}$ are the total transmission coefficient at the Fermi level which can be obtained by reversing the direction of the ferroelectric polarization of the barrier layer.

## III. RESULTS AND DISCUSSION

### A. Sliding ferroelectricity in the bilayer $VSi_2N_4$

The monolayer $VSi_2N_4$ possesses a unique atomic structure consisting of seven layers arranged as N-Si-N-V-N-Si-N, resembling the 1$H$-phase $VN_2$ encapsulated by buckled SiN layers. Notably, this structure bears resemblance to the experimentally synthesized $MoSi_2N_4$ family [33]. The monolayer exhibits ferromagnetic exchange interaction due to the presence of broken time-reversal symmetry [35], which possesses a hexagonal lattice with the space group of $P\bar{6}m2$. In the case of the bilayer $VSi_2N_4$, the AB stacking configuration with the space group of $P3m1$ is considered in our simulations. We investigate the existence of out of plane ferroelectricity in the AB stacking bilayer $VSi_2N_4$, and the corresponding bistable states, named state I (AB stacking) and state II (BA stacking), are illustrated in Fig. 1. In state I displayed in Fig. 1(a), the N atoms of the upper layer align directly above the Si atoms in the lower layer, while the N atoms in the lower layer are positioned beneath the V atoms of the upper layer. This asymmetric interlayer structure gives rise to a spontaneous vertical ferroelectric polarization along the $-z$

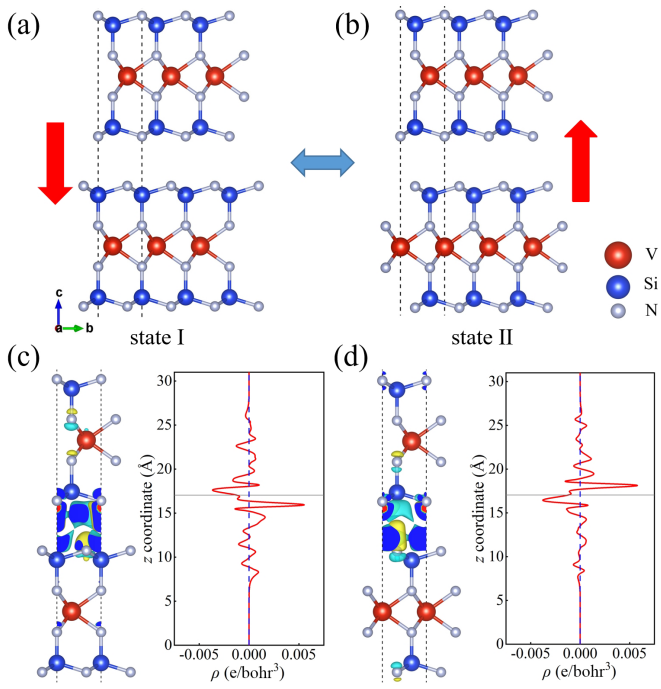


FIG. 1. (a), (b) Side views of bilayer $VSi_2N_4$ crystal structures in AB and BA stacking states, where red, blue, and silver spheres indicate the V, Si, and N atoms, respectively. The red arrows indicate the directions of ferroelectric polarization. Charge density differences and plane-averaged charge density differences along the $z$ direction of (c) state I and (d) state II, respectively. Yellow and blue regions represent electron accumulation and depletion, respectively. The isosurface value is set to 0.0001 $e/\text{Å}^3$.

direction. Furthermore, the polarization can be reversed by interlayer sliding to state II, in which the N atoms of the upper layer are right over the V atoms in the lower layer while the N atoms in the lower layer are below the Si atoms of the upper layer, leading to a spontaneous vertical ferroelectric polarization along the $+z$ direction, as shown in Fig. 1(b).

At the interface of the two Si-N layers, the net charge transfer due to the weak interlayer vdW interaction plays a crucial role in the generation of the spontaneous vertical polarization. To confirm the net charge transfer at the interface of the bilayer $VSi_2N_4$, the charge density differences between the upper and lower layers in state I and state II are illustrated in Figs. 1(c) and 1(d). The nonequivalence of charge in the accumulation and depletion regions leads to a net charge transfer between the two layers, giving rise to the vertical polarization. As depicted in the right panel of Fig. 1(c), the plane-averaged charge density difference along the $z$ direction in state I reveals a net charge transfer from the lower layer to the upper layer, resulting in the spontaneous ferroelectric polarization along the $-z$ direction. Conversely, as illustrated in the right panel of Fig. 1(d), a net charge transfer occurs from the upper layer to the lower layer in state II, lending to the spontaneous ferroelectric polarization along the $+z$ direction.

The intrinsic ferroelectricity of the bilayer $VSi_2N_4$ is further confirmed by analyzing the plane-averaged electrostatic potential. As shown in Figs. 2(a) and 2(b), we observe the positive (negative) discontinuity of the electrostatic potential difference is 153 meV (–153 meV) between the vacuum levels of upper and lower layers, indicating the spontaneous vertical ferroelectric polarization along the $-z$ ($+z$) direction (labeled by red arrows) in the AB (BA) stacking bilayer $VSi_2N_4$. It is worth noting that the AB and BA stacking configurations possess the same energy [see Fig. 2(d)]. Consequently, the bilayer $VSi_2N_4$ exhibits the spontaneous vertical ferroelectricity. In comparison, it is shown that the electrostatic distribution in the AA stacking remains the same between the upper and lower layers, as displayed in Fig. 2(c). This indicates a $P$-symmetry protection structure, resulting in the absence of a net ferroelectric polarization.

To investigate the feasibility of sliding ferroelectricity in the bilayer $VSi_2N_4$, we calculated the ferroelectric switching pathways and energy barriers between state I and state II using the NEB method, as shown in Fig. 2(d). Due to the presence of rotation symmetry $C_{3z}$, the ferroelectric polarization can be switched by performing interlayer sliding operations along [1/3, 2/3, 0], [–2/3, −1/3, 0], or [1/3, −1/3, 0], denoted as path I (see Fig. S1(a) in the Supplemental Materials (SM) [53]). Additionally, the ferroelectric switching can be achieved through the interlayer sliding along the other three equivalent directions, namely, [−2/3, −4/3, 0], [4/3, 2/3, 0], [–2/3, 2/3, 0], denoted as path II (see Fig. S1(b) in the SM [53]). The energy barriers along path I and path II are found to be 13 and 70 meV per unit cell, respectively. Consequently, the ferroelectric switching in the bilayer $VSi_2N_4$ is more likely to occur along path I due to the lower energy barrier. The energy barrier of the bilayer $VSi_2N_4$ is smaller than that of bilayer $VS_2$ (about 20 meV/u.c.) [32]. The lower energy barrier indicates lower energy consumption of ferroelectric phase transition. Based on the Berry phase method, we determine that the ferroelectric polarizations for state I and state II are −3.31 and 3.31 pC/m, respectively, which is comparable to that of the bilayer BN (2.25 pC/m) [22]. To determine the stability of ferroelectricity in the $VSi_2N_4$ bilayer at room temperature, we perform *ab initio* molecular dynamics simulations using the $4 \times 4 \times 1$ supercell to confirm the thermal stability of ferroelectricity in the AB stacking bilayer $VSi_2N_4$. As illustrated in Fig. S2 in the SM [53], there is neither bond breaking nor obvious interlayer sliding in the simulation at 300 K after 5 ps, indicating the robust stability of the sliding ferroelectricity in the bilayer $VSi_2N_4$ above room temperature.

Phonon vibrations play a pivotal role in phase transitions, particularly in ferroelectric materials. Recently, the soft mode theory has emerged as a valuable tool for understanding conventional ferroelectric phase transitions. It provides insights into the mechanisms underlying these transitions. The dynamical stability of the two ferroelectric phases is confirmed through the analysis of the phonon spectra, as depicted in Fig. S3(a) in the SM [53] for the bilayer $VSi_2N_4$. Furthermore, we calculate the phonon dispersion spectrum for the paraelectric (PE) state, as shown in Fig. S3(b) in the SM [53]. This analysis reveals the presence of pronounced soft optical modes at the Brillouin zone center Γ point. The soft mode, with a frequency of 0.6 THz, is referred to as the FE soft mode, which is the crucial optical phonon mode for ferroelectric phase transition in the bilayer $VSi_2N_4$. This indicates that the PE state serves as the transition state along the FE switching pathway. This observation suggests that the FE soft mode

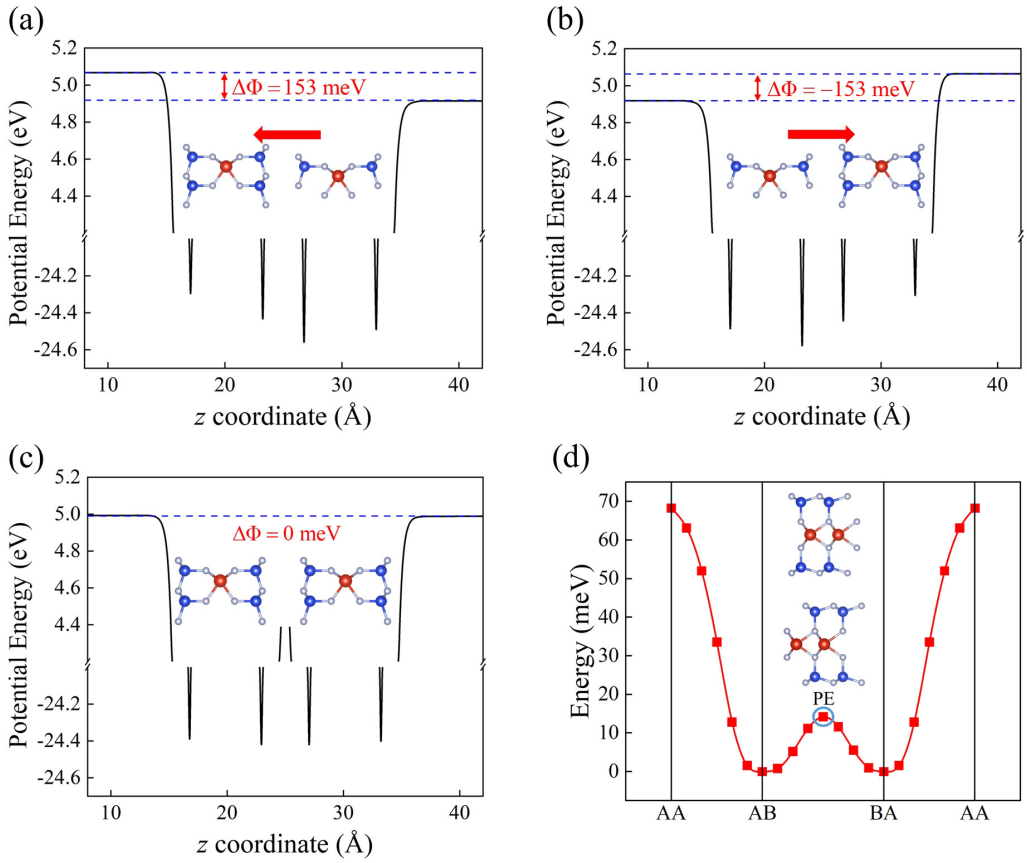


FIG. 2. The plane-averaged electrostatic potential of bilayer $VSi_2N_4$ under (a) AB stacking, (b) BA stacking, and (c) AA stacking along the $z$ direction. The insets describe the corresponding stacking structures. (d) Ferroelectric switching pathways and energy barriers through interlayer sliding in bilayer $VSi_2N_4$. The inset describes the geometry structure of the paraelectric (PE) state.

theory is applicable to the FE switching phenomenon in the bilayer $VSi_2N_4$.

### B. *A*-type antiferromagnetism

It is evident that the monolayer $VSi_2N_4$ exhibits ferromagnetic behavior, as demonstrated in recent theoretical studies [35]. To confirm the magnetic ground state of the bilayer $VSi_2N_4$, we considered both interlayer ferromagnetism and antiferromagnetism in our simulations for AB stacking configuration. Three different magnetic configurations are illustrated in Fig. 3(a), denoted as the ferromagnetic (FM), antiferromagnetic-1 (AFM1), and antiferromagnetic-2 (AFM2) states, respectively. Our total-energy calculations reveal that the AFM1 and AFM2 states, with degenerate energies 0.04 meV per unit cell lower than that of FM configuration, represent the magnetic ground state, forming *A*-type antiferromagnetism. The interlayer magnetic coupling is weak due to the small energy difference between the two interlayer magnetic orders. In terms of atomic distances of magnetic atoms, the distance of the nearest intralayer V-V atoms is $d_{AA} = 2.88$ Å, while the distance of the nearest interlayer V-V atoms is $d_{AB} = 9.69$ Å, resulting in strong intralayer ferromagnetic coupling and weak interlayer *A*-type antiferromagnetic coupling. Therefore, the interlayer magnetic order is susceptible to switching under an applied external field. When the transport direction is parallel to the layers, it is expected that Néel spin currents will occur in this direction. Therefore, the bilayer $VSi_2N_4$ exhibits *A*-type antiferromagnetism, composed of antiparallel aligned ferromagnetic layers, which is a candidate for the generation of layer-resolved spin Néel currents. More intriguingly, the band structure without considering the SOC of the AFM1 state reveals a significant spin splitting between the spin-up and spin-down channels due to the presence of spontaneous ferroelectric polarization, as illustrated in Fig. 3(b). The layer-resolved density of state (LDOS) indicates that the conduction band minimum (CBM) is primarily contributed by the spin-down channel of the upper layer while the valence band maximum (VBM) is primarily contributed by the spin-up channel of the lower layer. Conversely, in the AFM2 state, as illustrated in Fig. 3(c), the spin channels and LDOS have the opposite directions compared to the AFM1 state. Hence, the electronic properties of the bilayer $VSi_2N_4$ exhibit simultaneous spin splitting and layer-resolved characteristics, suggesting that the layer degree of freedom is coupled with the band edge and spin.

### C. Multiferroic coupling

We have successfully demonstrated that the bilayer $VSi_2N_4$ exhibits multiferroicity with the coexistence of both sliding ferroelectricity and weak interlayer *A*-type antiferromagnetism. To investigate the magnetoelectric coupling,

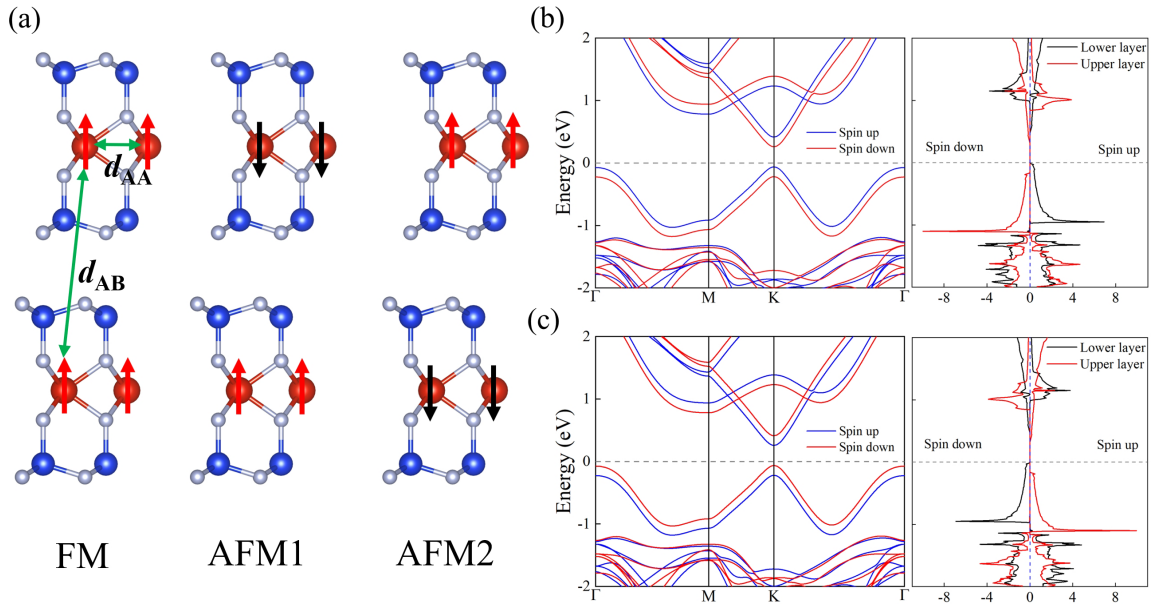


FIG. 3. (a) Three different magnetic configurations of bilayer $VSi_2N_4$ in ferromagnetic (FM), interlayer antiferromagnetic-1 (AFM1), and interlayer antiferromagnetic-2 (AFM2). Green arrows represent the nearest intralayer ($d_{AA}$) and interlayer ($d_{AB}$) distance of magnetic atoms. Red and black arrows represent the different spin directions of magnetic atoms. The spin-polarized band structures without spin-orbit coupling (SOC) and layer-resolved density of states are displayed for (b) AFM1 configuration and (c) AFM2 configuration.

four different ferroelectric/antiferromagnetic configurations, namely, $P\downarrow M\uparrow\downarrow$, $P\downarrow M\downarrow\uparrow$, $P\uparrow M\uparrow\downarrow$, and $P\uparrow M\downarrow\uparrow$ (see Fig. S4 in the SM [53]) are considered in our simulations, where $P\uparrow$ and $P\downarrow$ represent the ferroelectric polarization directions toward the $+z$ and $-z$ directions, respectively, and $M\uparrow\downarrow$ represents the magnetic orders of the upper and lower layers along the positive and negative directions of the $z$ axis. Remarkably, our results reveal that these four configurations have degenerate energies, indicating the potential for multistate storage in the bilayer $VSi_2N_4$. For the conventional ferroelectric bistable states, the electronic band structures should also be indistinguishable. However, in the case of the bilayer $VSi_2N_4$, the broken $T$ symmetry and $P$ symmetry lead to the emergence of spontaneous valley polarization. As a result, the electronic band structure becomes distinguishable, offering additional possibilities for manipulating and controlling the electronic properties of the bilayer systems. The inclusion of the SOC effect in calculations breaks the degeneracy at the $+K$ and $-K$ points, resulting in distinct energy levels and the appearance of spontaneous valley polarization due to the coupling between spin and momentum.

The spin-polarized band structures of the four different configurations with SOC are show in Figs. 4(a) and 4(b). We show that the $P\uparrow M\uparrow\downarrow$ and $P\downarrow M\downarrow\uparrow$ configurations exhibit identical band structures, as illustrated in Fig. 4(a). In these configurations, the CBM and VBM bands arise from opposite spin channels (the CBM is contributed by the spin-down channel and the VBM is contributed by the spin-up channel), exhibiting as a bipolar magnetic semiconductor with a band gap of 0.28 eV. Moreover, the VBM is located at the $+K$ point with energy higher than that of the $-K$ point, leading to a significant valley polarization of 64 meV, as illustrated in Fig. 4(c). Meanwhile, the CBM is situated at the $-K$ point with a lower energy compared to the $+K$ point, resulting in a spontaneous valley polarization of 1.5 meV. These findings are consistent with the previously reported values for the AA′ stacking bilayer $VSi_2N_4$ [28]. More intriguingly, if we just change the direction of the magnetic moment or the direction of the ferroelectric polarization to get the $P\uparrow M\downarrow\uparrow$ and $P\downarrow M\uparrow\downarrow$ configurations, the spin channels at the VBM and CBM and the valley polarizations of $-64$ and $-1.5$ meV are opposite simultaneously as depicted in Figs. 4(b) and 4(d). It is worth noting that the energy valleys $+K$ and $-K$ are related to each other by time-reversal symmetry rather than translational symmetry in valley materials. The band structure, which represents the energy levels and dispersion relationship of electrons in the material, plays a fundamental role in determining its electronic properties. From the perspective of qualitative definition of band structure, this is the indirect evidence that ferroelectric control of magnetism is achieved by ferrovalley coupling. Thus, when the ferroelectric polarization of the bilayer $VSi_2N_4$ is switched, the direction of magnetic moments in the upper and bottom layers needs to flip 180° to keep the band structure unchanged.

The breaking of $P$ symmetry and $T$ symmetry in the bilayer $VSi_2N_4$ leads to nonzero Berry curvature (BC) at the $+K$ and $-K$ points in the valleys. The BC is defined as [54]

$$\Omega_z(k) = -\sum_n \sum_{n\neq m} f_n(k) \frac{2\mathrm{Im}\langle\psi_{nk}|\hat{v}_x|\psi_{mk}\rangle\langle\psi_{nk}|\hat{v}_y|\psi_{mk}\rangle}{(E_{nk}-E_{mk})^2},$$

where $f_n(k)$ is the Fermi-Dirac distribution function with $k$ being the electron wave vector; $E_{nk}$ and $E_{mk}$ are the eigenvalues of the Bloch wave functions $\psi_{nk}$ and $\psi_{mk}$; $\hat{v}_x$ and $\hat{v}_y$ are velocity operators of the Dirac electrons; and $n$ and $m$

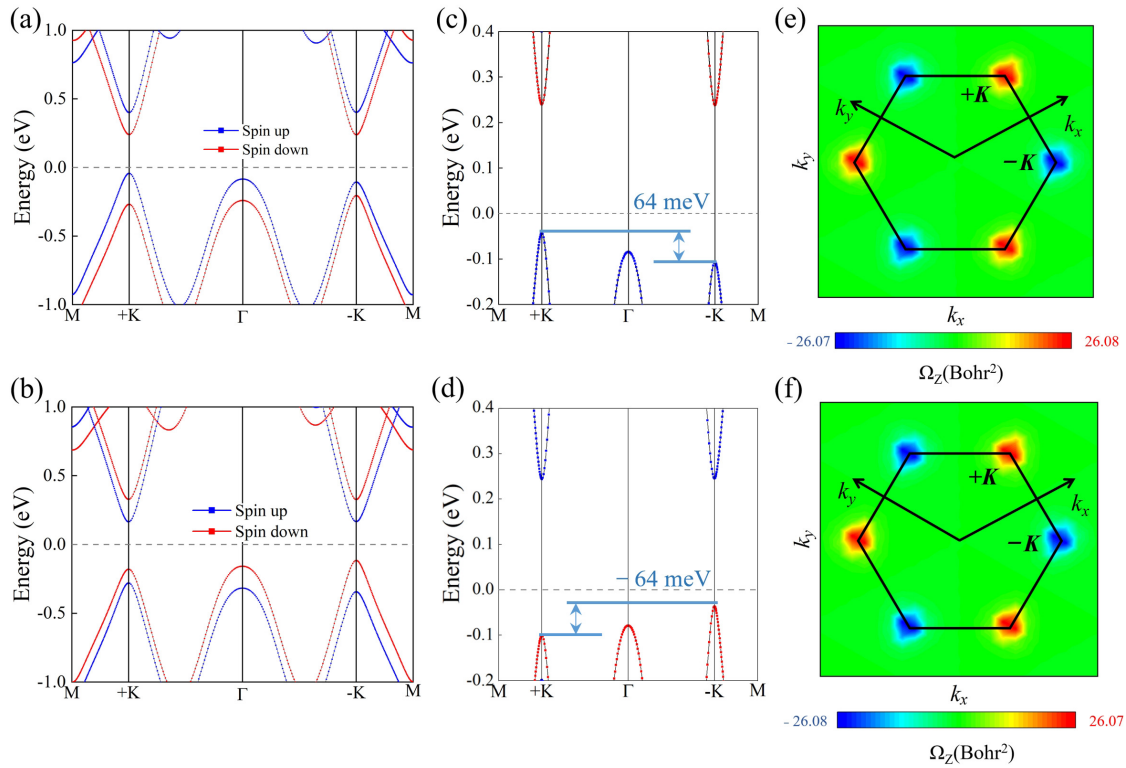


FIG. 4. (a) The band structure and (c) the enlarged low-energy band structure and (e) Berry curvatures with SOC of ferroelectric antiferromagnetic configurations $P\uparrow M\uparrow\downarrow$ and $P\downarrow M\downarrow\uparrow$. (b) The band structure and (d) the enlarged low-energy band structure and (f) Berry curvatures with SOC of configurations $P\uparrow M\downarrow\uparrow$ and $P\downarrow M\uparrow\downarrow$. The Fermi level is set to 0 eV. The blue (red) colors represent the bands of the spin projection in the positive (negative) directions of the $z$ axis (spin-up or spin-down).

are the band indices. To confirm the distinct Berry curvatures (BCs) in the four different configurations, we calculate the BCs using the VASPBERRY code as shown in Figs. 4(e) and 4(f). In the $P\uparrow M\uparrow\downarrow$ and $P\downarrow M\downarrow\uparrow$ configurations, the BCs at the $+K$ and $-K$ valleys exhibit opposite signs and unequal magnitudes with values of $-26.07$ and $+26.08$ bohrs$^2$, respectively. Meanwhile, in the $P\uparrow M\downarrow\uparrow$ and $P\downarrow M\uparrow\downarrow$ configurations, the BCs are $-26.08$ and $+26.07$ bohrs$^2$ at the $+K$ and $-K$ valleys, respectively. Thus, when the ferroelectric polarization is switched, the magnetic moments in the upper and lower layers need to be reversed to maintain the unchanged BCs. This provides further evidence that ferroelectric control of magnetism is achieved through ferrovalley coupling in the bilayer $VSi_2N_4$. In our simulations, there is a net magnetic moment of about $-0.003\,\mu_B$ when the SOC effect is considered without the external field. More intriguingly, the net magnetic moment will be switched to $0.003\,\mu_B$ with the reversal of the ferroelectric polarization, which is the direct evidence for the magnetoelectric coupling. Furthermore, in the presence of an in-plane electric field $E$, the Berry curvature will give the Bloch electrons an anomalous Hall velocity $v_\perp$, which is equal to $-\frac{e}{\hbar E}\Omega_z(K)$, resulting in the generation of an anomalous valley Hall effect. In addition, the magnetoelectric coupling of the bilayer $VSi_2N_4$ is intimately connected to the advantageous transport properties in $VSi_2N_4$ vdW MFTJs. These characteristics offer additional control mechanisms, such as ferroelectric switching and magnetoelectric coupling, to modulate the tunneling properties, spin-dependent transport, and, ultimately, the TER and TMR effects in these junctions.

### D. TMR and TER effects based on BLVSN in equilibrium state

After confirming the multiferroicity of the bilayer $VSi_2N_4$ (BLVSN), we can construct MFTJs using it as barrier layer. As mentioned earlier, there are a small energy barrier for the FE switching and weak interlayer AFM coupling in BLVSN, making it an ideal candidate for next-generation devices with lower power consumption. It is known that metallic Ag and Au are the most commonly used electrodes in device experiments. The optimized in-plane lattice parameters for the BLVSN, Au(111), and Ag(111) surfaces are 2.886, 2.898, and 2.904 Å, respectively. Considering the slight differences in lattice constants, the in-plane lattice mismatches at the interfaces of Au(111)/BLVSN and Ag(111)/BLVSN are 0.4% and 0.6%, respectively. Therefore, the Au(111) and Ag(111) surfaces are the suitable electrode materials for designing MFTJs based on BLVSN. To determine the heterojunction interfaces between the metal (111) surface and BLVSN, three types of interfaces are taken into consideration, denoted as metal-N, metal-Si, and metal-V as shown in Fig. 5(a). According to the calculations of the total energies for the three different interfaces, we find that the metal-N configurations for Au(111) and Ag(111) are the energy favorite configurations of the Au(111)/BLVSN and Ag(111)/BLVSN heterojunction interfaces, as illustrated in Fig. 5(b).

By performing full atomic relaxations of the MFTJs, as illustrated in Figs. 5(c) and 5(d), we construct vdW asymmetry MFTJs device, denoted as the Au(111)/BLVSN/Ag(111) model, where Au(111) and Ag(111) serve as the left and

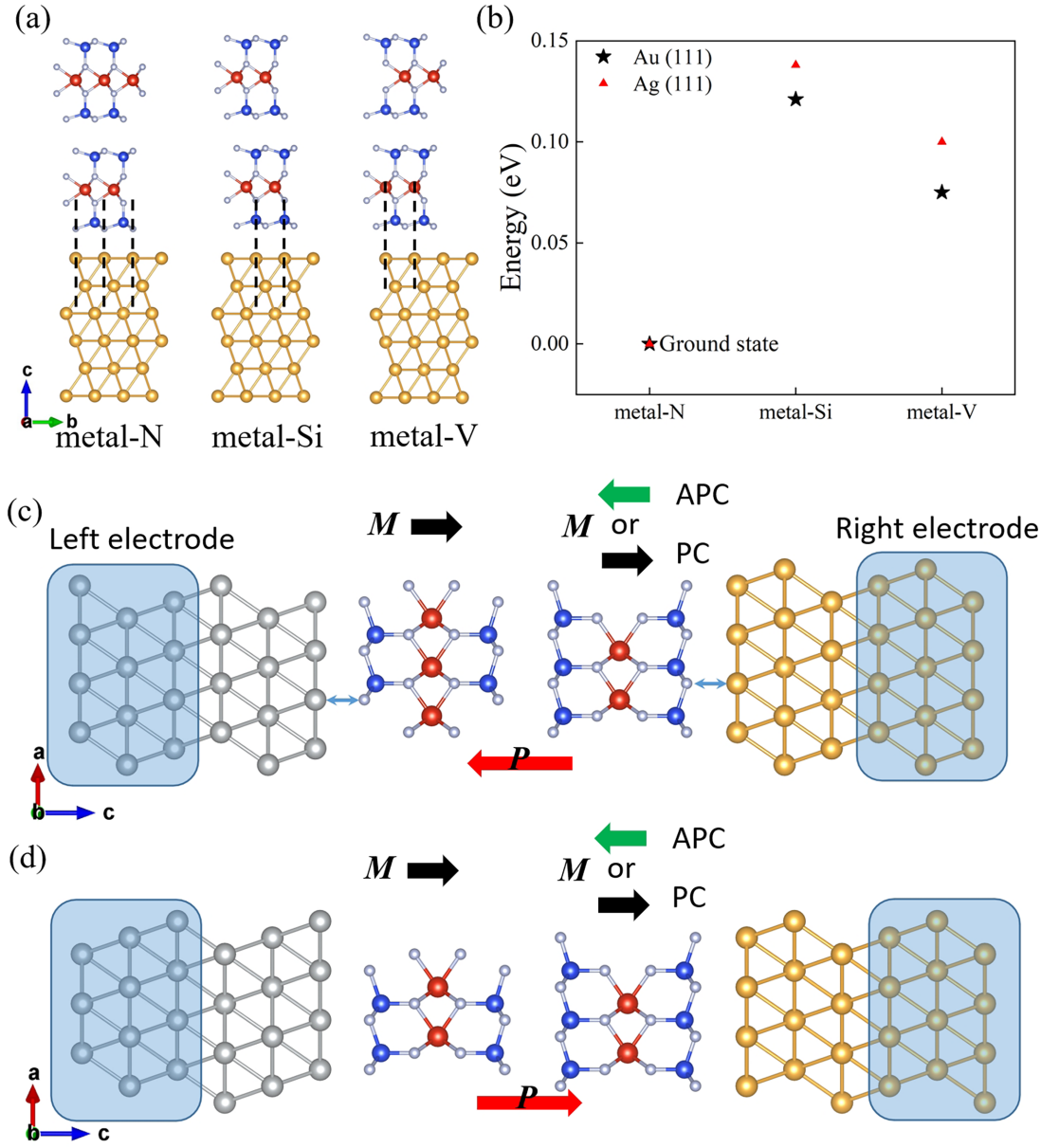


FIG. 5. (a) Three different stacking orders of metal/BLVSN interfaces, i.e., metal-N, metal-Si, and metal-V interfaces. (b) The relative total energy of three different interfaces of Ag(111) and Au(111). Schematic diagrams of Ag(111)/BLVSN/Au(111) MFTJs devices with (c) AB stacking BLVSN and (d) BA stacking BLVSN using Ag(111) as the left electrode and Au(111) as the right electrode. The left and right electrodes extend to semi-infinity. These devices are periodic in the *xy* plane and the current flows in the *z* direction.

right electrodes, respectively, and the BLVSN acts as the barrier layer. The optimized distances of the Ag-N and Au-N bonds at the two interfaces are 2.53 and 2.61 Å, respectively, indicating vdW interactions at these interfaces. This asymmetry in the two interfaces is crucial for the functioning of the MFTJs. Due to the underlying physical mechanisms of MTJs and FTJs, the magnetic direction of the BLVSN can be switched, resulting in two opposite magnetic orders [parallel configuration (PC) and antiparallel configuration (APC)], while the ferroelectric polarization of the BLVSN can be reversed by interlayer sliding, suggesting that four states can be induced in the MFTJs. As presented in Table I, when the ferroelectric polarization is downward (AB stacking), the TMR value is $7.84 \times 10^4\%$. Meanwhile, with the upward FE polarization (BA stacking), the TMR value increases to $1.01 \times 10^5\%$. This indicates that the TMR ratio in our MFTJs depends on the FE polarization of the BLVSN. Meanwhile, our results show that the spin injection efficiency ($\eta$) of these MFTJs for the PC state approaches 100% at zero bias voltage, which is the key factor for the ideal large TMR ratios. Another important factor in evaluating the performance of the MFTJs is the TER effect. With the reversal of the ferroelectric polarization from upward to downward through interlayer sliding, the TER values of the PC and APC magnetic orders are 7.5% and 37.7%, respectively. Therefore, the MFTJs exhibit favorable TMR and TER ratios, demonstrating significant potential for nonvolatile memory devices.

TABLE I. Calculated spin-dependent electron transmission $T\uparrow$ and $T\downarrow$, TMR, TER, and spin injection efficiency $\eta$ at the equilibrium state for Ag(111)/BLVSN/Au(111) MFTJs. $T_{tot} = T\uparrow + T\downarrow$.

| | PC ($M\uparrow\uparrow$) | | | | APC ($M\uparrow\downarrow$) | | | | |
|---|---|---|---|---|---|---|---|---|---|
| | $T\uparrow$ ($\times 10^{-6}$) | $T\downarrow$ ($\times 10^{-2}$) | $T_{tot}$ ($\times 10^{-2}$) | $\eta$ | $T\uparrow$ ($\times 10^{-5}$) | $T\downarrow$ ($\times 10^{-5}$) | $T_{tot}$ ($\times 10^{-5}$) | $\eta$ | TMR ($\times 10^{4}$%) |
| State I | 8.99 | 9.27 | 9.27 | ~100% | 1.86 | 9.96 | 11.80 | 69% | 7.84 |
| State II | 8.99 | 8.62 | 8.62 | ~100% | 3.95 | 4.62 | 8.57 | 8% | 10.11 |
| TER | | 7.5% | | | | 37.7% | | | |

### E. Significant TMR and TER effects based on TLVSN in equilibrium state

In order to further investigate the versatility and enhance the performance of MFTJs constructed from sliding multiferroics, we consider using the trilayer $VSi_2N_4$ (TLVSN) as the barrier layer to construct MFTJs. As depicted in Fig. 6(a), there are four different configurations of the directions of the ferroelectric polarizations in the TLVSN, denoted as the downward-FE state (down-FE), upward-FE state (up-FE), tail to tail AFE state (t-AFE) and head to head AFE state (h-AFE). The only difference among these states lies in the interlayer stacking orders, with corresponding ABC stacking, CBA stacking, BAB stacking, and ABA stacking, respectively. The energy differences between these four states are less than 1.0 meV, indicating that four states can undergo phase transitions with each other. We calculated the transition paths and energy barriers between these states as shown in Fig. 6(b); the small transition energy barriers between these states of

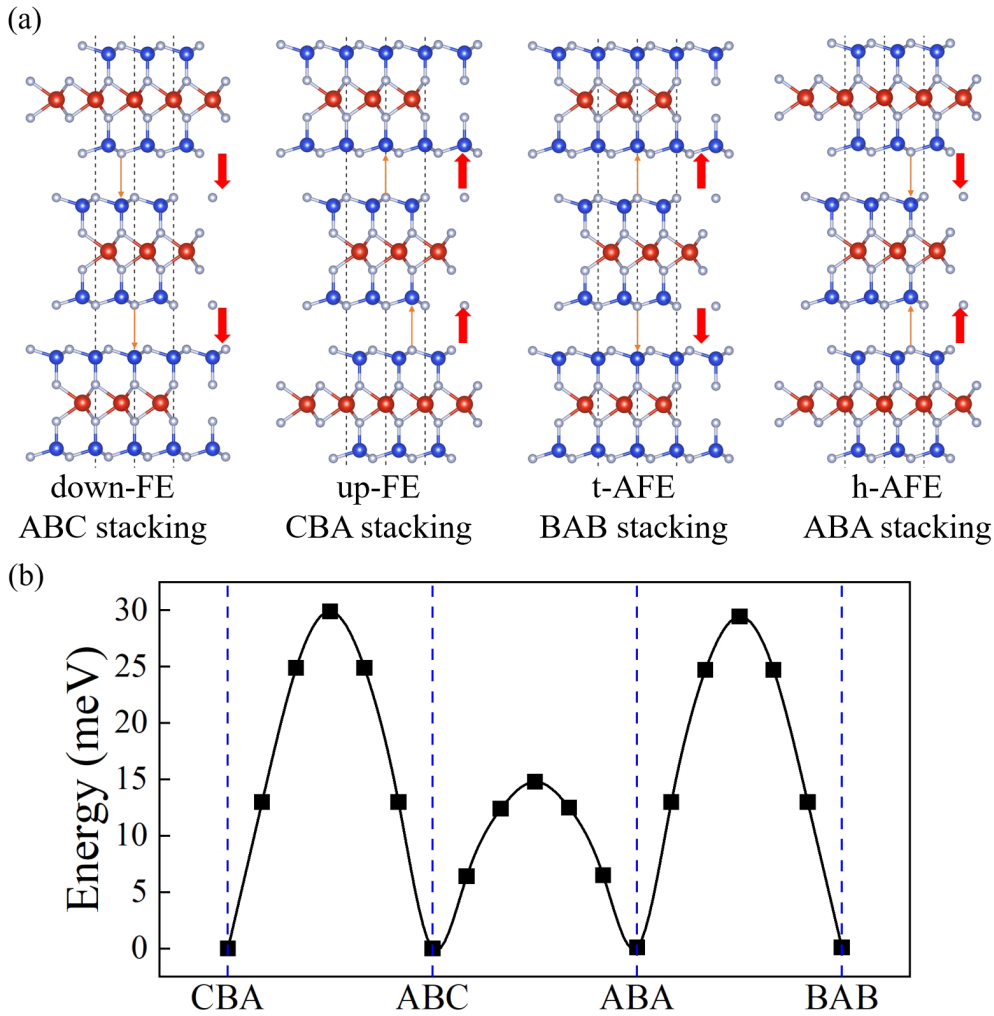


FIG. 6. (a) The crystal structures of TLVSN with four different ferroelectric configurations (ferroelectric polarizations are indicated by red arrows), i.e., down-FE (ABC stacking), up-FE (CBA stacking), t-AFE (BAB stacking), and h-AFE (ABA stacking). (b) The switching pathways and energy barriers of the four different ferroelectric configurations. The left and right electrodes extend to semi-infinity. The *xy* plane is periodic and in a hexagonal lattice and the current flows in the *z* direction for these MFTJs.

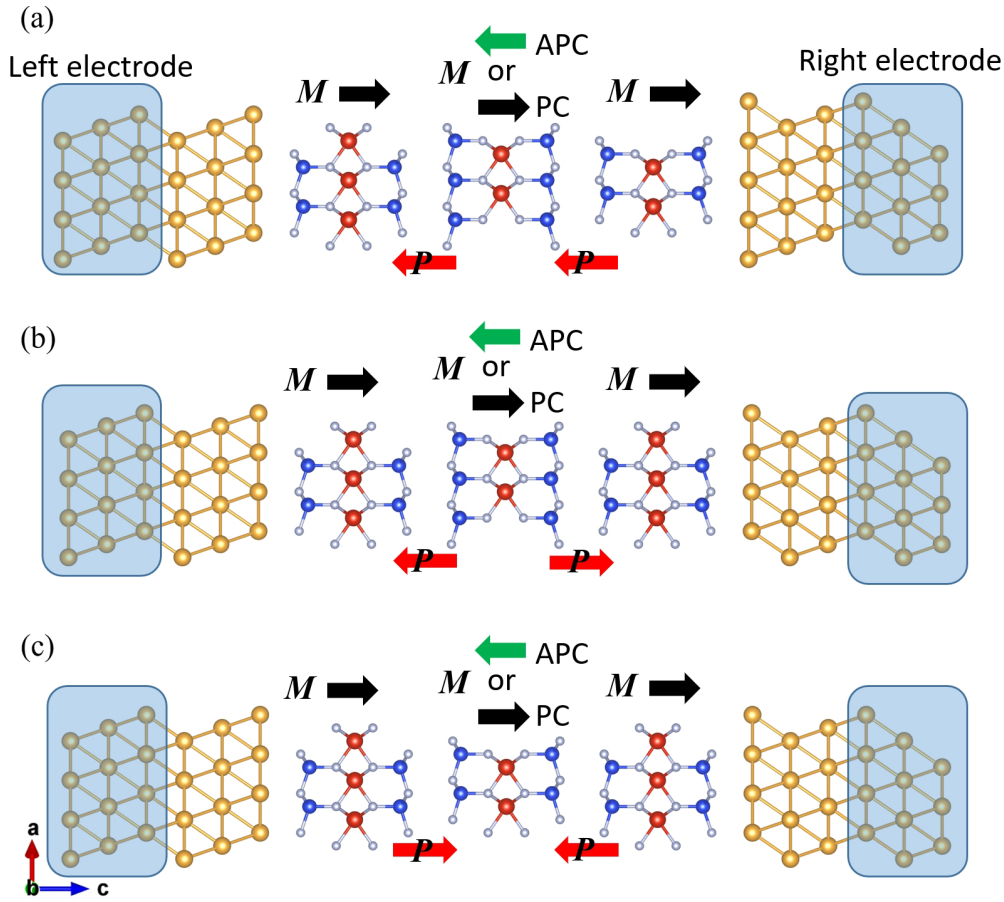


FIG. 7. Schematic diagrams of two-probe Au(111)/TLVSN/Au(111) MFTJ devices with three different out of plane FE polarization directions of (a) down-FE, (b) t-AFE, and (c) h-AFE with Au(111) as the left and right electrodes.

about 30 meV per unit cell, which are comparable to the ferroelectric switching barriers of conventional 3D perovskite oxides, indicate the feasibility of phase transitions between these states. Moreover, it is noteworthy that the ferroelectric polarization of TLVSN is about 6.8 pC/m, which is twice that of BLVSN, indicating that the ferroelectric polarization of the $VSi_2N_4$ increases linearly with the number of layers.

We consider the symmetric vdW MFTJs, where the TLVSN barrier layers separate the identical Au(111) electrodes, and electron transport occurs perpendicular to the plane of the junction, as depicted in Fig. 7. As evident from Table II, it is noteworthy that the TMR ratio depends on the ferroelectric polarization of TLVSN, and the considerable TMR ratios for the up-FE, h-AFE, and t-AFE states are $5.68 \times 10^3$, $5.55 \times 10^3$, and $5.08 \times 10^3$%, respectively. More importantly, we find that the magnetic order reversal of TLVSN mainly affects the transmission of the spin-down channel electrons due to changes in the electronic structures of the PC and APC near the Fermi level, which are mostly contributed by the spin-down electrons. The TMR ratios in our MFTJs are sufficiently large for implementation in spintronic devices, such as magnetic sensors and hard disk read heads. Considering the small energy difference between the up-FE, h-AFE, and t-AFE states, we evaluate the TER ratio based on symmetric MFTJs. There are three nonequivalent resistance states in our TER ratio simulations, corresponding to the

TABLE II. Calculated spin-dependent electron transmission $T\uparrow$ and $T\downarrow$, TMR, TER, and spin injection efficiency $\eta$ at the equilibrium state for Au(111)/TLVSN/Au(111) MFTJs. $T_{tot} = T\uparrow + T\downarrow$.

| | PC ($M\uparrow\uparrow\uparrow$) | | | | APC ($M\uparrow\downarrow\uparrow$) | | | | |
|---|---|---|---|---|---|---|---|---|---|
| | $T\uparrow$ ($\times 10^{-9}$) | $T\downarrow$ ($\times 10^{-3}$) | $T_{tot}$ ($\times 10^{-3}$) | $\eta$ | $T\uparrow$ ($\times 10^{-8}$) | $T\downarrow$ ($\times 10^{-5}$) | $T_{tot}$ ($\times 10^{-5}$) | $\eta$ | TMR ($\times 10^3$%) |
| h-AFE | 2.29 | 3.42 | 3.42 | ~100% | 2.52 | 6.06 | 6.06 | ~100% | 5.55 |
| FE | 4.39 | 7.95 | 7.95 | ~100% | 2.27 | 13.70 | 13.70 | ~100% | 5.68 |
| t-AFE | 4.82 | 1.45 | 1.45 | ~100% | 2.18 | 2.80 | 2.80 | ~100% | 5.08 |
| TER (h-AFE/FE) | | 137.7% | | | | 126.1% | | | |
| TER (t-AFE/FE) | | 448.3% | | | | 389.3% | | | |

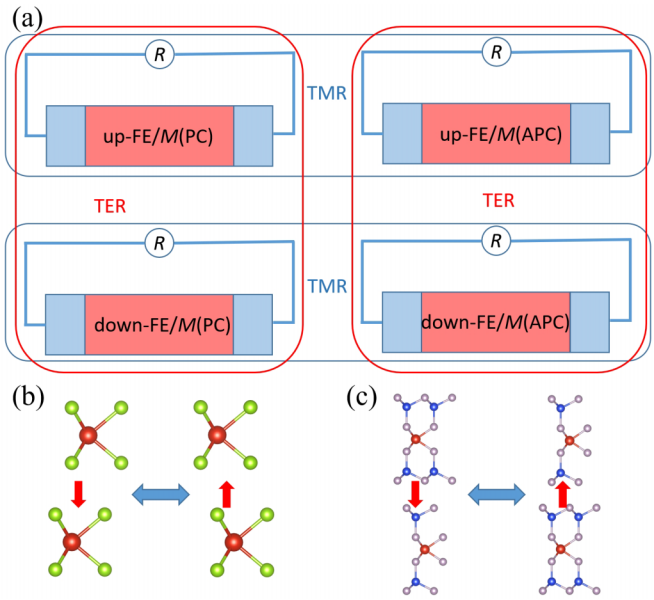


FIG. 8. (a) Schematic diagrams of MFTJs with sliding multiferroics. Blue regions are the left and right electrodes using suitable metallic materials. Red regions are the scattering region using sliding multiferroics. The mechanism of MFTJs can be extended to other sliding multiferroics, (b) bilayer $VS_2$ and (c) bilayer $VSi_2P_4$.

different barriers of the three states. As shown in Table II, the total transmission coefficient for the ferroelectric state is the largest among the three ferroelectric or antiferroelectric polarizations states. The AFE-FE phase transition enables direct control of the tunneling barrier height, resulting in a relatively large TER ratio. When the ferroelectric polarization is switched to the h-AFE state by sliding the top layer from ABC stacking to ABA stacking, the TER ratio in the PC (APC) magnetic state is 137.7% (126.1%). Meanwhile, when the FE polarization is switched to the t-AFE state by sliding the bottom later from ABC stacking to BAB stacking, the TER ratio in the PC (APC) magnetic state is 448.3% (389.3%). The TER ratio of the symmetric MFTJs based on TLVSN is an order of magnitude larger than that of the asymmetric MFTJs based on BLVSN. Thus, MFTJs with significant TER ratios may have great potential applications in nonvolatile resistance devices [see Fig. 8(a)]. Moreover, the unique design of the MFTJs based on layered sliding multiferroics can be extended to other 2D sliding multiferroics, such as $VS_2$ and $VSi_2P_4$ bilayers [32,37], as depicted in Figs. 8(b) and 8(c). This mechanism opens up possibilities for designing MFTJ devices and enables multistate storage.

## IV. SUMMARY

In summary, based on the first-principles density functional theory, we have proposed that bilayer $VSi_2N_4$ is intrinsic multiferroic with both spontaneous vertical ferroelectric polarization and interlayer antiferromagnetism. The multiferroic coupling of ferroelectricity and antiferromagnetism in the bilayer $VSi_2N_4$ can be achieved by a ferrovalley, resulting in electrically controlled magnetism. We can design switching of four different ferroelectric-antiferromagnetic configurations, which provides a possibility for realizing multistate storage. Furthermore, based on the density functional theory combined with the nonequilibrium Green's function method, we have theoretically revealed the spin-dependent electronic transport properties of asymmetric Au(111)/BLVSN/Ag(111) and symmetric Au(111)/TLVSN/Au(111) vdW MFTJs. We have observed a significant TMR ratio of up to $5.68 \times 10^3\%$ in the MFTJs by altering the magnetic orders of the trilayer $VSi_2N_4$ from parallel configuration (PC) to antiparallel configuration (APC) arrangement, as well as a large TER ratio of up to 448.3% through ferroelectric-antiferroelectric order transitions of the trilayer $VSi_2N_4$. The unique design of vdW MFTJs based on the layered multiferroic $VSi_2N_4$ can be extended to other sliding multiferroics ($VSi_2P_4$ and $VS_2$ bilayers), opening avenues for great opportunities for these multifunctional devices.

## ACKNOWLEDGMENTS

We acknowledge partial financial support from the Natural Science Foundation of Hubei Province (Grant No. 2022CFB927), the National Natural Science Foundation of China (Grant No. 12004021) and the Beijing Natural Science Foundation (Grant No. 4232070). We thank the Shanxi Supercomputing Center of China and TianHe-2 for providing computational resources.

[1] M. Gajek, M. Bibes, S. Fusil, K. Bouzehouane, J. Fontcuberta, A. Barthélémy, and A. Fert, Tunnel junctions with multiferroic barriers, Nat. Mater. **6**, 296 (2007).

[2] M. Fang, S. Zhang, W. Zhang, L. Jiang, E. Vetter, H. N. Lee, X. Xu, D. Sun, and J. Shen, Nonvolatile multilevel states in multiferroic tunnel junctions, Phys. Rev. Appl. **12**, 044049 (2019).

[3] C.-G. Duan, S. S. Jaswal, and E. Y. Tsymbal, Predicted magnetoelectric effect in $BaTiO_3$ multilayers: Ferroelectric control of magnetism, Phys. Rev. Lett. **97**, 047201 (2006).

[4] T. R. Paudel and E. Y. Tsymbal, Spin filtering in $CrI_3$ tunnel junctions, ACS Appl. Mater. Interfaces **11**, 15781 (2019).

[5] J. S. Moodera, L. R. Kinder, T. M. Wong, and R. Meservey, Large magnetoresistance at room temperature in ferromagnetic thin film tunnel junctions, Phys. Rev. Lett. **74**, 3273 (1995).

[6] X. Wang, C. Zhu, Y. Deng, R. Duan, J. Chen, Q. Zeng, J. Zhou, Q. Fu, L. You, S. Liu, J. H. Edgar, P. Yu, and Z. Liu, Van der Waals engineering of ferroelectric heterostructures for long-retention memory, Nat. Commun. **12**, 1109 (2021).

[7] J. P. Velev, C.-G. Duan, K. D. Belashchenko, S. S. Jaswal, and E. Y. Tsymbal, Effect of ferroelectricity on electron transport in $Pt/BaTiO_3/Pt$ tunnel junctions, Phys. Rev. Lett. **98**, 137201 (2007).

[8] S. Manipatruni, D. E. Nikonov, C. C. Lin, T. A. Gosavi, H. Liu, B. Prasad, Y. L. Huang, E. Bonturim, R. Ramesh, and L. A. Young, Scalable energy-efficient magnetoelectric spin–orbit logic, Nature (London) **565**, 35 (2019).

[9] L. Zhang, Y. Wang, X. Liu, and F. Liu, Electrical switching of spin-polarized current in multiferroic tunneling junctions, npj Comput. Mater. **8**, 197 (2022).

[10] M. Y. Zhuravlev, S. Maekawa, and E. Y. Tsymbal, Effect of spin-dependent screening on tunneling electroresistance and tunneling magnetoresistance in multiferroic tunnel junctions, Phys. Rev. B **81**, 104419 (2010).

[11] J. P. Velev, C.-G. Duan, J. D. Burton, A. Smogunov, M. K. Niranjan, E. Tosatti, S. S. Jaswal, and E. Y. Tsymbal, Magnetic tunnel junctions with ferroelectric barriers: Prediction of four resistance states from first principles, Nano Lett. **9**, 427 (2009).

[12] C. Wang, L. You, D. Cobden, and J. Wang, Towards two-dimensional van der Waals ferroelectrics, Nat. Mater. **22**, 542 (2023).

[13] D. L. Duong, S. J. Yun, and Y. H. Lee, van der Waals layered materials: Opportunities and challenges, ACS Nano **11**, 11803 (2017).

[14] Z. Cui, B. Sa, K.-H. Xue, Y. Zhang, R. Xiong, C. Wen, X. Miao, and Z. Sun, Magnetic-ferroelectric synergic control of multilevel conducting states in van der Waals multiferroic tunnel junction towards in-memory computing, Nanoscale **16**, 133 (2023).

[15] X. Dong, X. Shen, X. Sun, Y. Bai, Z. Yan, and X. Xu, Voltage-tunable giant nonvolatile multiple-state resistance in sliding-interlayer ferroelectric *h*-BN van der Waals multiferroic tunnel junction, Phys. Rev. B **108**, 085427 (2023).

[16] Y. Su, X. Li, M. Zhu, J. Zhang, L. You, and E. Y. Tsymbal, Van der Waals multiferroic tunnel junctions, Nano Lett. **21**, 175 (2021).

[17] W. Yang, Y. Cao, J. Han, X. Lin, X. Wang, G. Wei, C. Lv, A. Bournel, and W. Zhao, Spin-filter induced large magnetoresistance in 2D van der Waals magnetic tunnel junctions, Nanoscale **13**, 862 (2021).

[18] J. Han, C. Lv, W. Yang, X. Wang, G. Wei, W. Zhao, and X. Lin, Large tunneling magnetoresistance in van der Waals magnetic tunnel junctions based on $FeCl_2$ films with interlayer antiferromagnetic couplings, Nanoscale **15**, 2067 (2023).

[19] X. Lin, W. Yang, K. L. Wang, and W. Zhao, Two-dimensional spintronics for low-power electronics, Nat. Electron. **2**, 274 (2019).

[20] Z. Yan, Z. Li, Y. Han, Z. Qiao, and X. Xu, Giant tunneling magnetoresistance and electroresistance in $In_2Se_3$-based van der Waals multiferroic tunnel junctions, Phys. Rev. B **105**, 075423 (2022).

[21] Z. Yan, X. Jia, X. Shi, X. Dong, and X. Xu, Barrier-dependent electronic transport properties in two-dimensional $MnBi_2Te_4$-based van der Waals magnetic tunnel junctions, Appl. Phys. Lett. **118**, 223503 (2021).

[22] L. Li and M. Wu, Binary compound bilayer and multilayer with vertical polarizations: Two-dimensional ferroelectrics, multiferroics, and nanogenerators, ACS Nano **11**, 6382 (2017).

[23] Q. Yang, M. Wu, and J. Li, Origin of two-dimensional vertical ferroelectricity in $WTe_2$ bilayer and multilayer, J. Phys. Chem. Lett. **9**, 7160 (2018).

[24] C. Boix-Constant, S. Jenkins, R. Rama-Eiroa, E. J. G. Santos, S. Mañas-Valero, and E. Coronado, Multistep magnetization switching in orthogonally twisted ferromagnetic monolayers, Nat. Mater. **23**, 212 (2024).

[25] N. Sivadas, S. Okamoto, X. Xu, C. J. Fennie, and D. Xiao, Stacking-dependent magnetism in bilayer $CrI_3$, Nano Lett. **18**, 7658 (2018).

[26] K. Liu, X. Ma, S. Xu, Y. Li, and M. Zhao, Tunable sliding ferroelectricity and magnetoelectric coupling in two-dimensional multiferroic MnSe materials, npj Comput. Mater. **9**, 16 (2023).

[27] Y. Feng, Y. Dai, B. Huang, L. Kou, and Y. Ma, Layer Hall effect in multiferroic two-dimensional materials, Nano Lett. **23**, 5367 (2023).

[28] L. Liang, Y. Yang, X. Wang, and X. Li, Tunable valley and spin splittings in $VSi_2N_4$ bilayers, Nano Lett. **23**, 858 (2023).

[29] X. Ying, M. Ye, and L. Balents, Current switching of valley polarization in twisted bilayer graphene, Phys. Rev. B **103**, 115436 (2021).

[30] M. V. Stern, Y. Waschitz, W. Cao, I. Nevo, K. Watanabe, T. Taniguchi, E. Sela, M. Urbakh, O. Hod, and M. B. Shalom, Interfacial ferroelectricity by van der Waals sliding, Science **372**, 1462 (2021).

[31] K. Yasuda, X. Wang, K. Watanabe, T. Taniguchi, and P. Jarillo-Herrero, Stacking-engineered ferroelectricity in bilayer boron nitride, Science **372**, 1458 (2021).

[32] X. Liu, A. P. Pyatakov, and W. Ren, Magnetoelectric coupling in multiferroic bilayer $VS_2$, Phys. Rev. Lett. **125**, 247601 (2020).

[33] Y.-L. Hong, Z. Liu, L. Wang, T. Zhou, W. Ma, C. Xu, S. Feng, L. Chen, M.-L. Chen, D.-M. Sun, X.-Q. Chen, H.-M. Cheng, and W. Ren, Chemical vapor deposition of layered two-dimensional $MoSi_2N_4$ materials, Science **369**, 670 (2020).

[34] Q. Cui, Y. Zhu, J. Liang, P. Cui, and H. Yang, Spin-valley coupling in a two-dimensional $VSi_2N_4$ monolayer, Phys. Rev. B **103**, 085421 (2021).

[35] Y. Feng, Z. Wang, X. Zuo, and G. Gao, Electronic phase transition, spin filtering effect, and spin Seebeck effect in 2D high-spin-polarized $VSi_2X_4$ ($X$= N, P, As), Appl. Phys. Lett. **120**, 092405 (2022).

[36] T. Zhong, Y. Ren, Z. Zhang, J. Gao, and M. Wu, Sliding ferroelectricity in two-dimensional $MoA_2N_4$ ($A$ = Si or Ge) bilayers: High polarizations and Moiré potentials, J. Mater. Chem. A **9**, 19659 (2021).

[37] T. Zhang, X. Xu, B. Huang, Y. Dai, L. Kou, and Y. Ma, Layer-polarized anomalous Hall effects in valleytronic van der Waals bilayers, Mater. Horiz. **10**, 483 (2023).

[38] B. Hammer, L. B. Hansen, and J. K. Nørskov, Improved adsorption energetics within density-functional theory using revised Perdew-Burke-Ernzerhof functionals, Phys. Rev. B **59**, 7413 (1999).

[39] K. Burke, J. P. Perdew, and M. Ernzerhof, Why the generalized gradient approximation works and how to go beyond it, Int. J. Quantum Chem. **61**, 287 (1997).

[40] S. Grimme, S. Ehrlich, and L. Goerigk, Effect of the damping function in dispersion corrected density functional theory, J. Comput. Chem. **32**, 1456 (2011).

[41] S. Grimme, J. Antony, S. Ehrlich, and H. Krieg, A consistent and accurate *ab initio* parametrization of density functional dispersion correction (DFT-D) for the 94 elements H–Pu, J. Chem. Phys. **132**, 154104 (2010).

[42] H. J. Monkhorst and J. D. Pack, Special points for Brillouin-zone integrations, Phys. Rev. B **13**, 5188 (1976).

[43] T. Fukui, Y. Hatsugai, and H. Suzuki, Chern numbers in discretized Brillouin zone: Efficient method of computing (spin) Hall conductances, J. Phys. Soc. Jpn. **74**, 1674 (2005).

[44] R. D. King-Smith and D. Vanderbilt, Theory of polarization of crystalline solids, Phys. Rev. B **47**, 1651 (1993).

[45] G. Henkelman, B. P. Uberuaga, and H. Jónsson, A climbing image nudged elastic band method for finding saddle points and minimum energy paths, J. Chem. Phys. **113**, 9901 (2000).

[46] S. Smidstrup, D. Stradi, J. Wellendorff, P. A. Khomyakov, U. G. Vej-Hansen, M. E. Lee, T. Ghosh, E. Jónsson, H. Jónsson, and K. Stokbro, First-principles Green's-function method for surface calculations: A pseudopotential localized basis set approach, Phys. Rev. B **96**, 195309 (2017).

[47] S. Smidstrup, T. Markussen, P. Vancraeyveld, J. Wellendorff, J. Schneider, T. Gunst, B. Verstichel, D. Stradi, P. A. Khomyakov, U. G. Vej-Hansen, M. E. Lee, S. T. Chill, F. Rasmussen, G. Penazzi, F. Corsetti, A. Ojanperä, K. Jensen, M. L. N. Palsgaard, U. Martinez, A. Blom *et al.*, Quantum ATK: An integrated platform of electronic and atomic-scale modelling tools, J. Phys.: Condens. Matter **32**, 015901 (2020).

[48] M. Brandbyge, J.-L. Mozos, P. Ordejón, J. Taylor, and K. Stokbro, Density-functional method for nonequilibrium electron transport, Phys. Rev. B **65**, 165401 (2002).

[49] Y. Meir and N. S. Wingreen, Landauer formula for the current through an interacting electron region, Phys. Rev. Lett. **68**, 2512 (1992).

[50] A.-P. Jauho, N. S. Wingreen, and Y. Meir, Time-dependent transport in interacting and noninteracting resonant-tunneling systems, Phys. Rev. B **50**, 5528 (1994).

[51] S. Yuasa, T. Nagahama, A. Fukushima, Y. Suzuki, and K. Ando, Giant room-temperature magnetoresistance in single-crystal Fe/MgO/Fe magnetic tunnel junctions, Nat. Mater. **3**, 868 (2004).

[52] L. L. Tao and J. Wang, Ferroelectricity and tunneling electroresistance effect driven by asymmetric polar interfaces in all-oxide ferroelectric tunnel junctions, Appl. Phys. Lett. **108**, 062903 (2016).

[53] See Supplemental Material at http://link.aps.org/supplemental/10.1103/PhysRevB.109.085433 for further details, including ferroelectric switching pathways, *ab initio* molecular dynamics simulation, phonon dispersion spectra, and four different ferroelectric/antiferromagnetic configurations for the bilayer $VSi_2N_4$.

[54] D. J. Thouless, M. Kohmoto, M. P. Nightingale, and M. den Nijs, Quantized Hall conductance in a two-dimensional periodic potential, Phys. Rev. Lett. **49**, 405 (1982).